An environmentally ultrasensitive fluorine probe to resolve protein conformational ensembles by ^{19}F NMR and cryo-EM

Yun Huang[1,2,*], Krishna Reddy[1], Clay Bracken[3], Biao Qiu[1], Wenhu Zhan[4], David Eliezer[3,*], Olga Boudker[1,2,*]

[1]Department of Physiology & Biophysics, Weill Cornell Medicine, 1300 York Ave, New York, NY 10021; [2]Howard Hughes Medical Institute, Chevy Chase; [3]Department of Biochemistry, Weill Cornell Medicine, 1300 York Ave, New York, NY 10021; [4]Department of Microbiology & Immunology, Weill Cornell Medicine, 1300 York Ave, New York, NY 10065, United States

* To whom correspondence should be addressed: olb2003@med.cornell.edu; dae2005@med.cornell.edu; yuh2010@med.cornell.edu

Abstract

Limited chemical shift dispersion represents a significant barrier to studying multi-state equilibria of large membrane proteins by ^{19}F NMR. We describe a novel monofluoroethyl ^{19}F probe that dramatically increases the chemical shift dispersion. The improved conformational sensitivity and line shape enable the detection of previously unresolved states in 1D NMR spectra of a 134 kDa membrane transporter. Changes in the populations of these states in response to ligand binding, mutations, and temperature correlate with population changes of distinct conformations in structural ensembles determined by single-particle cryo-electron microscopy. Thus, ^{19}F NMR can guide sample preparation to discover and visualize novel conformational states and facilitate image analysis and 3D classification.

Introduction

The functions of numerous membrane proteins, including transporters, channels, and receptors, require conformational transitions. Insights into the structure and dynamics of the functional states are crucial for mechanistic understanding and therapeutic development [1-3]. Crystallography and single-particle cryogenic electron microscopy (cryo-EM) can provide structural snapshots of different states in a protein ensemble, while various bulk [4] and single-molecule [5-7] approaches can report on dynamics. Nuclear magnetic resonance (NMR) spectroscopy is a powerful tool for studying the dynamics of small proteins. However, NMR sensitivity and resolution decline with protein size, and probing the dynamics of proteins over 100 kDa, including membrane proteins, by NMR remains challenging.

1D ^{19}F NMR using site-specific probes can be effective for this purpose because of its high sensitivity, the absence of background signals, the exquisite responsiveness of ^{19}F chemical shifts to conformational changes, and its compatibility with inexpensive low-field instruments [8-10]. Furthermore, 1D ^{19}F NMR is a single-pulse experiment with no heteronuclear magnetization transfer. It can therefore quantify state populations of even weak or broad resonances. The unique advantages of ^{19}F NMR have led to wide-ranging applications in studying membrane protein dynamics [9, 11], protein aggregation [12], protein behavior in cells [13], and drug screening [14]. Commonly used ^{19}F probes include aromatic fluorine and trifluoromethyl groups. The latter show faster longitudinal and slower transverse relaxation rates due to fast rotation, leading to higher sensitivity [15]. Manglik et al. developed a trifluoromethyl phenyl group, where the phenyl ring functions as a chemical shift dispersion amplifier [16-17]. However, the chemical shift dispersion of trifluoromethyl-based probes generally does not exceed 2 ppm [16, 18-20], resulting in severe resonance overlap in large proteins. Recently, Boeszoermenyi et al. reported ^{19}F-^{13}C TROSY, improving resonance dispersion via a second dimension [21], but sacrificing the advantages of the 1D experiment. Therefore, developing ^{19}F probes with improved dispersion, i.e., increased environmental sensitivity, remains a challenge and is essential for expanding ^{19}F NMR applications [17, 22-23].

Herein, we report a novel cysteine-conjugated ^{19}F monofluoroethyl (mFE) probe exhibiting narrow linewidths and ultrahigh sensitivity to conformational changes with chemical shift dispersion reaching 9 ppm.

^{19}F chemical shifts of aliphatic monofluorides depend on C-C-C-F dihedral angles in addition to local electric fields and van der Waals interactions [24 25]. In a trifluoroalkyl probe, all rotamers are equivalent, but in the monofluoroalkyl probe, the *gauche*- and *anti*-rotamers, which can exhibit chemical shift differences of up to 14 ppm [25] are not equivalent. Because of the low energy barrier separating the rotamers, they exchange much faster than the NMR time scale [26], giving a population-weighted chemical shift. We hypothesized that for an mFE probe, weak ^{19}F interactions with the local environment of distinct protein conformations might affect the equilibrium of the *gauche* and *anti*-isomers, giving rise to different population-weighted chemical shifts and larger chemical shift dispersions than for a trifluoroethyl (tFE) probe. Such weak interactions should not significantly alter the kinetics of rotamer exchange, which would remain fast on the NMR time scale. Additionally, fluorine chemical shift anisotropy (CSA) is approximately two times lower in mFE than in the tFE group [27]. Because ^{19}F transverse relaxation depends quadratically on the CSA, mFE might feature slower relaxation and narrower linewidths.

To test the environmental sensitivity of the novel mFE probe, we used the aspartate transporter Glt_{Ph}, an excellent model protein because it samples several functional conformations with known structures. Glt_{Ph} is similar in size to or larger than many membrane receptors, channels, and transporters. As an archaeal homolog of human glutamate transporters, it harnesses energy from sodium gradients to transport aspartate via an “elevator” mechanism [28]. It is an obligate homotrimer of 134 kDa molecular weight that can be reconstituted as a protein-micelle particle of ~300 kDa [29]. During transport, the three Glt_{Ph} protomers function independently [30], undergoing conformational transitions between the outward- and inward-facing states (OFS and IFS), where the substrate-binding site can open to the extracellular solution and cytoplasm, respectively. ^{19}F NMR measurements using mFE-labeled Glt_{Ph} resolve an unexpectedly complex conformational landscape, demonstrating the power of the new probe and prompting concordant cryo-EM studies that confirm multiple coexisting states. The response of the

84 dominant NMR signals to environmental changes, including temperature, correlates with
85 changes in the ensemble of structures determined by cryo-EM, allowing for provisional
86 assignments of some of the NMR signals to specific structural states. Importantly, our
87 data also suggest that cryo-EM can accurately reflect the effects of temperature and other
88 conditions on conformational equilibria in solution, a subject of considerable controversy.

89

90 **Results**

91 **High environmental sensitivity of the mFE probe**

92 We designed and synthesized deuterated ^{19}F labeling compounds S-(2-fluoroethyl-
93 1,1,2,2-D_4) and *p*-toluenethiosulfonate ($TsSCD_2CD_2F$) using commercially available
94 reagents (**Fig. 1a** and **b**). Deuterated probes provide sharper lines resulting from reduced
95 ^{19}F-^{2}H scalar couplings compared to ^{19}F-^{1}H couplings and from the elimination of ^{19}F-^{1}H
96 dipole relaxation at the cost of reduced sensitivity due to longer longitudinal relaxation
97 times (T_1) and relaxation delays. We then prepared single cysteine mutants, A380C,
98 A381C, and M385C, of a previously characterized fully functional cysteine-free Glt_{Ph}
99 variant (termed wild-type, WT, for brevity; see Methods for details and Ref. [20]) and a
100 variant with additional gain-of-function mutations R276S/M395R (termed RSMR). The
101 RSMR mutations accelerate transitions between OFS and IFS [20, 31] and substrate uptake
102 by ~8-fold [32]. Thiosulfonates are known to react with cysteine thiols selectively, rapidly,
103 and quantitatively (**Fig. 1c**) [33], and the observed efficiency of $TsSCD_2CD_2F$ reacting with
104 a single cysteine of Glt_{Ph} was near 100 % (**Fig. S1a**). All mFE-labeled mutants retained
105 transport activity when reconstituted into liposomes (**Fig. S1b**).

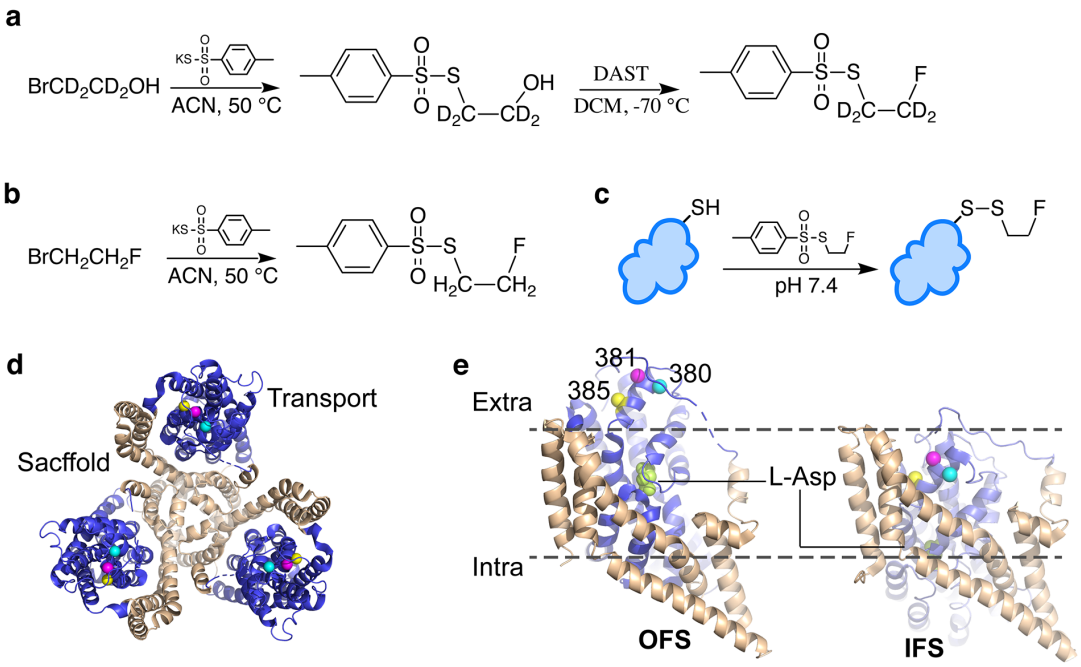

Figure 1. Synthesis of the mFE probes and site-specific protein labeling. Synthesis of ^{19}F deuterated and protonated mFE probes $TsSCD_2CD_2F$ (**a**) and $TsSCH_2CH_2F$ (**b**). (**c**) Cysteine-specific labeling. (**d**) The structure of the Glt_{Ph} trimer with scaffold domains is colored tan, and the transport domains are blue. Colored spheres show the sites of single cysteine mutations A380C (cyan), A381C (magenta), and M385C (yellow). (**e**) The elevator transition of the Glt_{Ph} transport domain from OFS (left) to IFS (right). Single protomers are shown in the membrane plane, represented by the dotted lines. The bound substrate aspartate is shown as lime spheres. ACN: acetonitrile; DAST: diethylaminosulfur trifluoride; DCM: dichloromethane; X: hydrogen or deuterium; Ts: Toluenesulfonyl.

We next compared the chemical shift dispersion of the deuterated mFE and its predecessor tFE probe. We recorded 1D ^{19}F spectra of mFE- and tFE-labeled WT-M385C and RSMR-M385C Glt_{Ph} in the presence of Na^+ ions and aspartate or a competitive blocker (3S)-3-[[3-[[4-(trifluoromethyl)benzoyl]amino]phenyl]methoxy]-L-aspartic acid (TFB-TBOA). As previously reported, the tFE probe exhibited three peaks with a chemical shift dispersion of 1.1 ppm (**Fig. 2a** and **S2a**) [20]. In contrast, the mFE spectra collectively featured five peaks, S1-S5, at 25 °C, with respective chemical shifts of ~ -214.8, 216.0, 216.6, 217.5, and 218.1 ppm (**Fig. 2b** and **S2b, c**). An analysis of three independently prepared samples showed that peak identification is highly reproducible, with only small deviations in the fitted peak positions, linewidths, and populations (**Fig. S3**). We ascribe the slight shift in the S4 peak in the presence of TFB-TBOA to a structural difference between the aspartate- and TFB-TBOA-bound transporters in the OFS [34]. When we

lowered the temperature below 15 °C to slow down conformational transitions, we observed an additional S6 peak at ~ -218.5 ppm for RSMR-M385C-mFE (**Fig. S2**). Overall, the mFE resonances covered a range of 3.6 ppm. Ligands, mutations, and temperature affect the S1-S6 peak populations, suggesting that the resonances correspond to distinct structural states of the transporter and that their populations reflect the kinetic and equilibrium properties of the conformational ensemble. The three Glt_{Ph} protomers function independently [30, 35], and the labeling positions on the adjacent protomers are too distant to affect each other (**Fig. 1d**). Therefore, the ^{19}F resonances report on the structural states of individual protomers.

We also compared tFE- and mFE-labeled WT-A380C and WT-A381C Glt_{Ph} mutants bound to Na^+ ions only or Na^+ ions and aspartate (**Fig. 2c, d** and **Fig. S4**). For both labeling sites, the mFE probe resulted in wider chemical shift dispersion. Strikingly, WT-A380C-mFE featured 7 peaks distributed over 8.9 ppm (**Fig. 2d**), demonstrating the tremendous potential of the probe. To our knowledge, this is the broadest chemical shift dispersion observed and the greatest number of protein states simultaneously resolved using ^{19}F NMR.

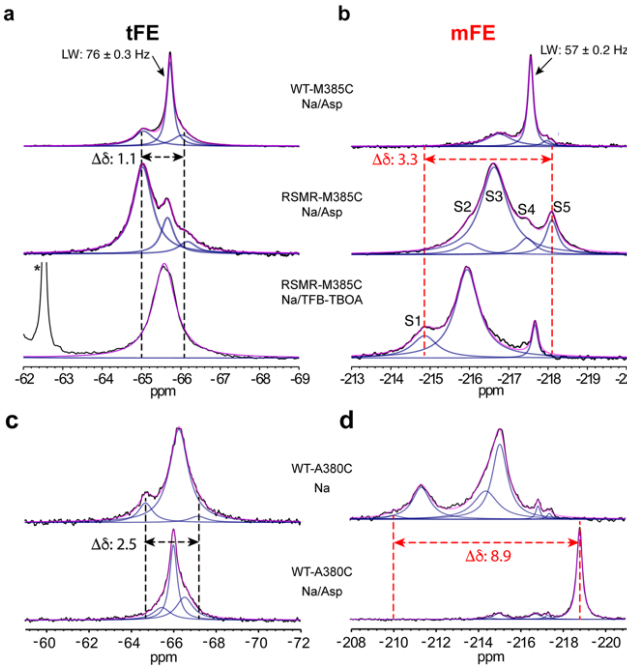

Figure 2. mFE-labeled Glt_{Ph} variants show wide chemical shift dispersion. ^{19}F NMR spectra of Glt_{Ph}-M385C (**a**, **b**) and Glt_{Ph}-A380C (**c**, **d**) labeled with tFE (**a**, **c**) and mFE (**b**, **d**). From top to bottom: WT and RSMR mutant in 100 mM Na^+ and 2 mM aspartate (Asp), the RSMR mutant in 100 mM Na^+ and 0.6 mM TFB-TBOA (**a**, **b**), and WT in 400 mM Na^+ and 100 mM Na^+ and 2 mM aspartate (**c**, **d**). All spectra were recorded at 25 °C. Raw data are black, fitted spectra are pink, and deconvoluted Lorentzian peaks are blue. The asterisk denotes a signal from the CF_3 group of TFB-TBOA. S1-S5 denote resolved resonances of Glt_{Ph}-M385C-mFE. $\Delta\delta$ is the largest chemical shift difference observed for the labeling site. All ^{19}F NMR spectra here and elsewhere were recorded at least twice on independently prepared protein samples, producing similar results.

136 **^{19}F-guided cryo-EM imaging to discover new conformational states**

137 The ultrahigh environmental sensitivity of the mFE probe enables monitoring of how
138 conformational equilibria are perturbed by the physicochemical environment, ligands, and
139 mutations. Moreover, it can reveal hitherto uncharacterized structural states. For example,
140 the ^{19}F NMR spectra of WT-M385C-mFE and RSMR-M385C-mFE bound to the
141 competitive blocker DL-*threo*-β-benzyloxyaspartic acid are dominated by distinct peaks,
142 S4 for WT and S2 for RSMR (TBOA, **Fig. 3a**). Thus, unexpectedly, TBOA stabilizes the
143 WT and RSMR transporters in different conformations. To establish whether these
144 resonances correspond to OFS or IFS, we examined their solvent accessibility using
145 paramagnetic relaxation enhancement (PRE). M385 is solvent-exposed in OFS but
146 buried on the interface between the transport and scaffold domains in IFS (**Fig. 1e**) [34, 36].
147 The addition of the soluble paramagnetic reagent Gd-DTPT-BMA significantly broadened
148 the S4 but much less the S2 peak of the TBOA-bound RSMR mutant (**Fig. S5a**).
149 Therefore, we assigned S4 to OFS and S2 to IFS. Similarly, for the Na^+-bound WT, the
150 paramagnetic reagent broadened S4 but not S2 or S3 (**Fig. S5b**), confirming the
151 assignments of S4 and indicating that S3 is also IFS. The observation that the S2 and S3
152 peaks are intrinsically broader than S4 is also consistent with the faster transverse
153 relaxation expected for a buried M385 site in these states.

154 Our ^{19}F NMR data revealed that the blocker TBOA stabilized the WT transporter in OFS,
155 consistent with the published cryo-EM structure of this state [34]. Unexpectedly, however,
156 the blocker appeared to stabilize the RSMR mutant in an unknown IFS state. Motivated
157 by this paradox, we imaged TBOA-bound RSMR by cryo-EM. Following particle alignment
158 with imposed C3 symmetry, we performed symmetry expansion and 3D classification to
159 sort multiple conformations of the transporter protomers [34, 37]. We observed 91 %
160 protomers in IFS with a wide-open substrate-binding site occupied by TBOA (**Fig. 3b**, **Fig.
161 S6,** and **Table S1**; see *Methods* for data processing details). The remaining protomers
162 were in OFS, similar to the TBOA-bound WT (RMSD of 0.646 Å). Because S2 and S4 are
163 the only peaks in the RSMR-M385C-mFE NMR spectrum, we ascribe S2 to the highly
164 populated open IFS and S4 to the minor OFS population observed by cryo-EM.
165 Interestingly, the TBOA-bound WT populated a distinct S3 IFS (**Fig. 3a**). Consistently, a

166 cryo-EM structure of the TBOA-bound WT transporter constrained in IFS by crosslinking
167 showed a different, more closed conformation [34] than the structure we assigned to S2.
168 Thus, the previously unobserved S2 state reveals a new modality of the ligand interaction
169 with the transporter. While the physiological relevance of the S2 state is beyond the scope
170 of this paper, it could represent an open-gate intermediate in the substrate release
171 process.

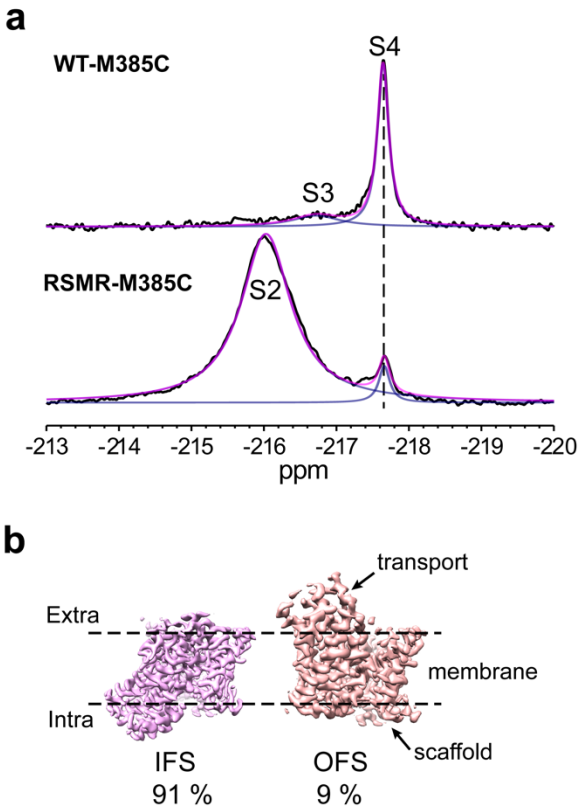

Figure 3. Identification and structural elucidation of new transporter conformations. (**a**) ^{19}F NMR spectra of WT-M385C-mFE (upper panel) and RSMR-M385C-mFE (bottom panel) in the presence of 100 mM NaCl and 2 mM TBOA. The resonances occurring with similar chemical shifts to those in Fig. 2 are labeled S2, S3, and S4. (**b**) Cryo-EM density maps of TBOA-bound RSMR Glt_{Ph} mutant protomers in IFS (left) and OFS (right) structural classes. The corresponding populations are below the maps.

172 **Synergistic use of ^{19}F NMR and cryo-EM in exploring the conformation landscape**

173 Under transport conditions in the presence of sodium and aspartate, ^{19}F NMR spectra of
174 RSMR-M385C-mFE showed that it populates a surprising number of conformational
175 states, manifesting as resonances S1-S6 (**Fig. 2b, Fig. S2b** and **S2c**). Temperature
176 modulated their populations so that, at 4 °C, we observed all states, with S6 being the
177 most populated, while above 15 °C, S3 became dominant and S6 invisible (**Fig. S2**).
178 Notably, the S6 peak decreased in amplitude and shifted to the left with increasing
179 temperature, suggesting that it exchanges with another peak with rates approaching the

NMR time scale of high μs to low ms. Solvent PRE at 15 °C, where S2 – S6 are well resolved, resulted in faster T_1 relaxations of S4 and S5 but not S2, S3, and S6 resonances (**Fig. 4** and **Fig. S7**), suggesting that the mFE probe is exposed to the solvent for the former states and buried in the latter. The S1 peak is too small to evaluate by PRE. These results suggest that the RSMR mutant visits at least two OFS-like conformations, S4 and S5, and three different IFSs, S2, S3, and S6, exchanging slower than the NMR time scale. These assignments are consistent with the S2, S3, and S4 assignments described above for the TBOA-bound and Na^+-bound transporters (**Fig. 3**, and **Fig. S6**)

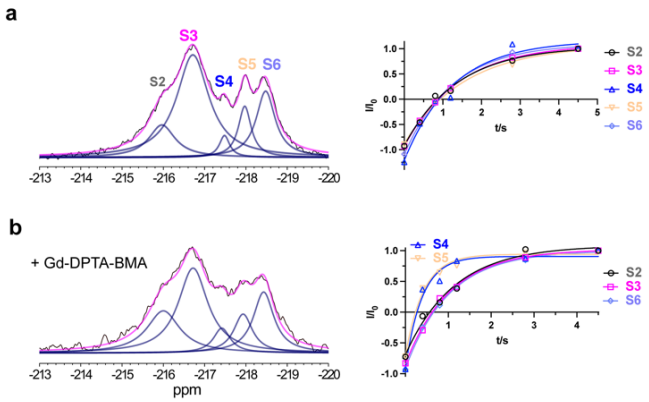

Figure 4. Assignment of IFS and OFS conformations based on solvent PRE effects. ^{19}F NMR spectra (left) were recorded, and T_1 relaxations (right) were measured in 300 mM NaCl and 2 mM Asp at 15 °C. Relaxation data were fitted to monoexponential functions (solid lines). The fitted T_1 values are 1.36 ± 0.20, 1.41 ± 0.02, 1.26 ± 0.33, 1.56 ± 0.16, and 1.26 ± 0.09 s for S2, S3, S4, S5, and S6, respectively, in the absence of Gd-DPTA-BMA (**a**) and 1.15 ± 0.20, 1.04 ± 0.08, 0.39 ± 0.08, 0.42 ± 0.06, and 1.01 ± 0.06 s in the presence of 20 mM Gd-DPTA-BMA (**b**). The error bars, estimated as described in *Methods*, are too small to see.

The temperature-dependent population changes observed in ^{19}F NMR experiments prompted us to ask whether cryo-EM can recapitulate them and inform the assignment of resonances to structural states. We flash-froze cryo-EM grids of RSMR-M385C-mET preincubated in 500 mM NaCl and 2 mM aspartate at 4, 15, and 30 °C. After data processing, 3D classification of protomers imaged at 4 °C revealed that ~87 % of them fell into IFS classes with variable orientations of the transport domain relative to the scaffold (**Fig. S8)**. The remaining ~13 % were in a previously described intermediate OFS (iOFS), in which the transport domain moves inward slightly compared to OFS. Based on similar transport domain positions, we grouped IFS classes into IFS-A and IFS-B ensembles with populations of 19 and 67 %, respectively (**Fig. 5 and Fig. S8a**). The main structural difference between them is that the transport domain packs more tightly against the scaffold in IFS-A but leans away and leaves a detergent-filled gap in IFS-B (**Fig. S8e**).

Similar structures were observed crystallographically and termed “locked” and “unlocked”, respectively [31]. The increasing temperature had little effect on the population of iOFS but led to a dramatic increase in IFS-A to ~ 82 % at 30 °C and a corresponding decrease in IFS-B populations to ~ 9 % (**Fig. 5c and Fig. S8b**).

The population shift from IFS-B to IFS-A at higher temperatures observed in cryo-EM parallels the increase of S3 and decrease of S6 in ^{19}F NMR (**Fig. 5a**), strongly suggesting that S3 corresponds to IFS-A and S6 to IFS-B (**Fig. 5c**). Notably, the RSMS trimer crystallized at 4 °C with two protomers in the “unlocked” IFS-B and one protomer in the “locked” IFS-A [31], consistent with the higher IFS-B population observed by NMR and cryo-EM at 4 °C. S4, which corresponds to OFS, is lowly populated in RSMR but dominant in the WT transporter (**Fig. 2b** and **3a**). Consistently, cryo-EM didn’t identify the OFS in 4 °C data set. Instead, we only found ~ 2 % of particles in OFS in the 15 °C cryo-EM data set, reflecting the challenge in cryo-EM of detecting lowly populated states. S5 likely corresponds to iOFS because it is the only other observed structural state with the solvent-exposed 385C residue. While these assignments are plausible based on solvent exposure and the correlated population changes in the NMR and cryo-EM data, they remain speculative in the absence of direct structural data, such as we previously used to assign NMR signals to OFS from iOFS [20]. The identities of the S1 and S2 resonances remain ambiguous. In particular, we did not observe a state in the cryo-EM classifications resembling the TBOA-bound RSMR structure, which populates the S2 peak (**Fig. 3**). Therefore, it is possible that one of the IFS conformations in the ensembles serendipitously shows a chemical shift similar to that of the TBOA-bound RSMR structure. The decrease in the S2 population at higher temperatures, thermodynamically similar to S6, suggests that it might correspond to one of the “unlocked” IFS-B subclasses.

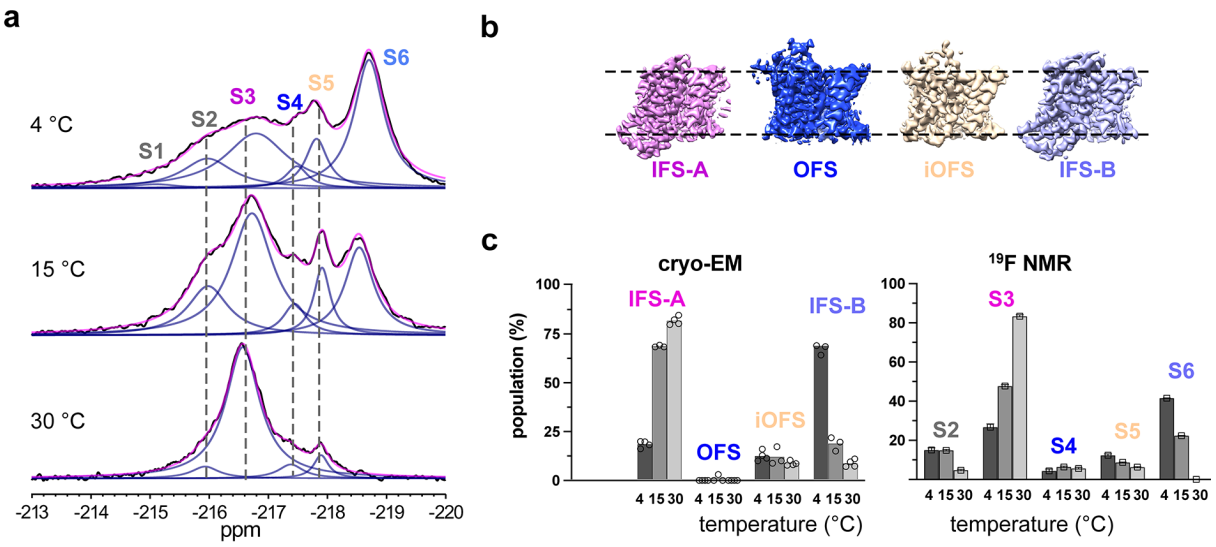

Figure 5. State populations observed in 3D classifications of protomers in cryo-EM parallel NMR measurements. (**a**) NMR spectra of RSMR-M385C-mFE were recorded in the presence of 500 mM NaCl and 2 mM Asp at 4 (top), 15 (middle), and 30 °C (bottom). (**b**) Representative maps of the four structural classes identified during cryo-EM particle 3D classifications of RSMR-M385C-mFE prepared at 4 °C. (**c**) The populations of protomers' 3D classes in samples preincubated at 4, 15, and 30 °C (left). Open circles are results obtained using different T values and numbers of classes during 3D classifications in Relion. The state populations measured in ^{19}F NMR experiments at the same temperatures are shown in the right panel. Errors are from multiple-peak deconvolutions of spectra in OriginPro.

Discussion

Despite decades of efforts to develop biophysical methods to study protein dynamics, monitoring changes in membrane protein samples with more than two states remains challenging. The model protein in this study is a 134 kDa membrane transporter, Glt_{Ph}, that undergoes complex conformational transitions to utilize transmembrane sodium ion gradients to drive the concentrative transport of aspartate. Resolving multi-conformational ensembles of such large membrane proteins using existing NMR methods is difficult. Our new mFE ^{19}F probe takes advantage of the unique electronic properties of the monofluoroalkyl group leading to ultrahigh environmental sensitivity. It achieves chemical shift dispersion of ~9 ppm in the case of Glt_{Ph}.

236 Relatively simple and inexpensive, ^{19}F NMR using the new probe is an excellent tool for
237 guiding high-resolution structural determinations by crystallography or cryo-EM. For
238 example, ^{19}F NMR showed that the transport blocker TBOA stabilizes the gain-of-function
239 RSMR mutant of Glt_{Ph} in a different conformation than the WT. Consequent cryo-EM
240 imaging led to the discovery of a novel conformation of the transporter in IFS featuring an
241 open substrate gate and a new mode of inhibitor binding.

242 ^{19}F NMR resonances are difficult to assign to specific structural states because their
243 chemical shifts are exquisitely sensitive to the local environment, indirectly reflecting
244 global protein conformations. Previously, we showed that transition metal-mediated
245 longitudinal PRE could assist with state assignments by evaluating the distance between
246 the ^{19}F label and a double histidine-coordinated metal ion. Here, we take advantage of
247 enhanced line broadening and T_1 relaxation due to the PRE effects of gadolinium
248 compounds in solution to distinguish states with buried and exposed mFE probes. These
249 measurements discriminate between OFS- and IFS-like states in WT Glt_{Ph} and its RSMR
250 mutant.

251 Protein solutions are plunge-frozen for cryo-EM imaging in a process thought to preserve
252 protein conformations, which can then be visualized by 3D classifications of the particles.
253 Factors such as protein adsorption to the grids, surface tension and temperature changes
254 during freezing may shift the conformation equilibrium. In addition, data processing, and
255 parameters used in classifications can affect the obtained populations of 3D classes [38].
256 Therefore, whether the class distributions reflect state populations in solutions is unclear.
257 Here, for the first time, we evaluated the reliability of the state populations obtained from
258 3D classifications of EM-imaged particles. We found that the state populations
259 determined by cryo-EM match well with those measured by ^{19}F NMR. For example, the
260 IFS and OFS populations of TBOA-bound RSMR were 95 and 5 % in ^{19}F NMR and 91
261 and 9 % in cryo-EM, respectively. There was also good correspondence in complex
262 ensembles of the aspartate-bound RSMR mutant preincubated at different temperatures.
263 We observed a temperature-dependent correlated population increase of the main S3
264 resonance and the cryo-EM IFS-A structural ensemble and a corresponding decrease in
265 the S6 resonance and the IFS-B ensemble.

266 Structural determination by cryo-EM and accurate state populations measured by ^{19}F
267 NMR provide a novel means to correlate the structural and thermodynamic properties of
268 membrane proteins. For example, our results suggest that IFS-B has a dramatically lower
269 enthalpy than IFS-A, resulting in the steep temperature dependence of the IFS-B to IFS-
270 A transition. The lower IFS-B enthalpy must be associated with breaking the protein
271 interface between the transport and scaffold domains and inserting detergent moieties
272 into the gap. The detailed analysis of the phenomenon is beyond the scope of the paper.
273 Nevertheless, our results show that even modest temperature changes can have
274 profound effects on the observed conformational ensemble of a membrane protein, a
275 feature characteristic, for example, of temperature-sensing ion channels[39]. ^{19}F NMR is
276 ideally suited to probe the temperature dependence of protein equilibria and might
277 facilitate the study of the thermodynamics of membrane proteins-bilayer interactions.

278 ^{19}F NMR can detect conformations of RSMS-M385C-mEF present at only a few percent,
279 such as the S4 peak, attributed to OFS. Such lowly populated states might be important
280 functional intermediates, yet they are difficult to isolate during 3D classification of cryo-
281 EM-imaged particles, especially when several conformations coexist. Thus, we only found
282 OFS in the 15 °C cryo-EM dataset, where ^{19}F NMR suggests its population is slightly
283 higher than at 4 or 30 °C and where we collected the largest number of particles.
284 Therefore, the ability of ^{19}F NMR to visualize rare states provides a means to assess their
285 populations and optimize conditions that can enrich them for high-resolution structural
286 elucidation.

287 In summary, mFE chemical shift dispersion significantly exceeds that of tFE, enabling a
288 more detailed and quantitative description of protein conformational ensembles and
289 guiding cryo-EM imaging. Improved peak separation should also facilitate measurements
290 of chemical exchange rates by methods such as EXSY [20] and saturation transfer,
291 including CEST [40]. Continuously expanding structural methodologies reveal that proteins
292 populate diverse conformational ensembles. For example, a G protein-coupled
293 adenosine A_{2A} receptor samples at least five distinguishable states during activation [41].
294 Our model protein is similar in size to or larger than many physiologically important

295 receptors, transporters, and ion channels. The new ^{19}F probe should greatly facilitate
296 mechanistic studies of such proteins.

297

298 **Materials and Methods**

299 **Synthesis of S-(2-fluoroethyl-1,1,2,2-D_4) *p*-toluenethiosulfonate**

300 To a solution of potassium *p*-toluenethiosulfonate (678 mg, *TCI Chemical*) in dry
301 acetonitrile (10 ml) was added 2-bromoethanol-1,1,2,2-d_4 (240 μl, *Cambridge Isotope*
302 *Laboratories*) under argon. The mixture was stirred at 60 °C overnight. The solvent was
303 evaporated under reduced pressure, and the residue was dissolved in 50 ml ethyl acetate
304 and washed with 0.5 M HCl aqueous solution (2 × 20 ml) and brine. The organic layer
305 was dried over anhydrous Na_2SO_4 and then evaporated under reduced pressure to give
306 S-(2-hydroxyethyl-1,1,2,2-D_4) *p*-toluenethiosulfonate (600 mg, 85 % yield) as an oil. The
307 product was directly used for the next step without further purification.

308 To a solution of S-(2-hydroxyethyl-1,1,2,2-D_4) *p*-toluenethiosulfonate (480 mg, 2 mmol)
309 in dry dichloromethane (5 ml) precooled to -70 °C, 1.5 equivalents of diethylaminosulfur
310 trifluoride (3 ml of 1 M solution in dichloromethane, *Sigma-Aldrich*) were added dropwise
311 under argon. After 10 min of stirring at -70 °C, the flask was warmed to room temperature
312 for 30 min. The reaction was quenched with 0.5 ml of methanol. The reaction mixture was
313 evaporated to dryness and then purified using a flash column (*RediSep Rf*) using 0-60 %
314 petroleum ether/ethyl acetate. The major fraction was collected and evaporated to obtain
315 the pure title compound (220 mg, 45 % yield). The identity of the compound was
316 confirmed by NMR. ^1H NMR (500 MHz, $CDCl_3$) δ 7.82 (d, J = 8.4 Hz, 2H), δ 7.36 (d, J =
317 7.7 Hz, 2H), δ 2.46 (s, 3H); ^{13}C NMR (125 MHz, $CDCl_3$) δ 145.40, 141.85, 130.18, 127.24,
318 81.44-79.32 (J = 171.19 Hz), 34.88 (m), 31.84; ^{19}F NMR (470 MHz, $CDCl_3$) δ -215.25 (m).

319 **Synthesis of S-(2-fluoroethyl) *p*-toluenethiosulfonate**

320 To a solution of potassium *p*-toluenethiosulfonate (620 mg, 2.7 mmol, *TCI Chemical*) in
321 dry acetonitrile (10 ml) 1-bromo-2-fluoroethane (203 μl, *Accela ChemBio Inc.*) was added

322 under argon. The mixture was stirred at 60 °C overnight. The solvent was removed under
323 reduced pressure, and the residue was dissolved in 50 ml ethyl acetate and washed with
324 0.5 M HCl aqueous solution (2 × 20 ml) and brine. The organic layer was dried over
325 anhydrous Na_2SO_4 and evaporated under reduced pressure. The residue was purified by
326 flash column chromatography to give the pure title compound (503 mg, 86 % yield) as an
327 oil. The identity of the compound was confirmed by NMR. ^{1}H NMR (500 MHz, $CDCl_3$) δ
328 7.82 (d, *J* = 8.2 Hz, 1H), 7.36 (d, *J* = 8.1 Hz, 1H), 4.61 (t, *J* = 6.3 Hz, 1H), 4.52 (t, *J* = 6.3
329 Hz, 1H), 3.30 (t, *J* = 6.3 Hz, 1H), 3.26 (t, *J* = 6.3 Hz, 1H), 2.46 (s, 3H); ^{13}C NMR (126 MHz,
330 $CDCl_3$) δ 145.22, 141.72, 130.01, 127.11, 81.01 (d, *J* = 172.6 Hz), 35.38 (d, *J* = 22.7 Hz),
331 21.70; ^{19}F NMR (471 MHz, $CDCl_3$) δ -213.51 (tt, *J* = 46.9, 20.4 Hz).

332 **Protein expression, purification, and labeling**

333 The single cysteine mutations A380C, A381C, and M385C were introduced into the
334 Y215H/E219H cysteine-free Glt_{Ph} mutant (termed WT here for brevity), where the
335 introduction of double histidine has been shown to not perturb the transport activity
336 significantly [20]. The M385C mutation was also introduced into the gain-of-function variant
337 generated by additional R276S/M395R mutations (RSMR for brevity). All constructs were
338 expressed, purified, and labeled as described, with modifications [20, 36]. In brief, pBAD
339 plasmids encoding constructs with C-terminal thrombin cleavage sites followed by $(His)_8$-
340 tag were transformed into *E. coli* DH10-B cells (*Invitrogen*). Cells were grown in LB media
341 at 37 °C to an OD_{600} of 1.1. The temperature was then set to 30 °C and protein expression
342 was induced by adding 0.2 % arabinose (*Goldbio*). Cells were grown for additional 16
343 hours. The cells were harvested by centrifugation and resuspended in 20 mM HEPES,
344 pH 7.4, 200 mM NaCl, 1 mM L-asp, and 1 mM EDTA. The suspended cells were broken
345 by an Emulsiflex C3 high-pressure homogenizer (*Avestin Inc.*) in the presence of 0.5
346 mg/ml lysozyme (*Goldbio*) and 1 mM phenylmethanesulfonyl fluoride (PMSF, *MP*
347 *Biomedicals*). After centrifugation for 15 min at 5,000 g, the supernatant was centrifuged
348 at 125,000 g for 50 min.

349 For mFE labeling, the membrane pellets were collected and solubilized in a buffer
350 containing 20 mM HEPES, pH 7.4, 200 mM NaCl, 1 mM Asp, 10 mM 2-mercaptoethanol,
351 40 mM n-dodecyl-β-D-maltopyranoside (DDM, *Anatrace, Inc.*) for 2 hours at 4 °C. The

352 mixture was centrifuged for 50 min at 125,000 g. The supernatant was diluted 3 times
353 with buffer A (20 mM HEPES, pH 7.4, 200 mM NaCl, 1 mM Asp) and incubated with Ni-
354 NTA resin (*Qiagen*) for 1 hour at 4 °C. The resin was washed with 6 volumes of Buffer A
355 supplemented with 1 mM DDM and 25 mM imidazole and proteins were eluted in buffer
356 A supplemented with 1 mM DDM and 300 mM imidazole. EDTA was added to the
357 collected protein fractions to a final concentration of 0.5 mM. The protein was
358 concentrated to ~10 mg/ml using concentrators with 100 kDa MW cutoff (*Amicon*). Protein
359 concentration was determined by UV absorbance at 280 nm using the extinction
360 coefficient of 57,400 M^{-1} cm^{-1} and MW of 44.7 kDa (protomer). Two molar equivalents of
361 $TsSCD_2CD_2F$ or $TsSCH_2CH_2F$, prepared as stock solutions in DMSO, were added to the
362 protein samples followed by incubation at 4 °C for 2 hours or room temperature for 1 hour.
363 Thrombin was added and incubated overnight at room temperature to cleave the $(His)_8$-
364 tag.

365 For tFE labeling, the membrane pellet was solubilized in a buffer containing 20 mM
366 HEPES, pH 7.4, 200 mM NaCl, 1 mM Asp, 40 mM DDM, and 2 mM 2,2'-dithiodipyridine
367 (DTDP, *Sigma Aldrich*). After binding to Ni-NTA resin, the protein-resin slurry was first
368 washed with 5 volumes of Buffer A supplemented with 1 mM DDM. Trifluoroethanethiol
369 (2 mM, *Sigma Aldrich*) was added, and the slurry was incubated with mixing at 4 °C
370 overnight. The resin was washed with buffer A supplemented with 1 mM DDM and 25
371 mM imidazole and then eluted with buffer A supplemented with 1 mM DDM and 300 mM
372 imidazole. The $(His)_8$-tag was cleaved using thrombin at room temperature overnight.

373 Both mFE- and tFE-labeled proteins were further purified by size exclusion
374 chromatography (SEC) using a Superdex 200 Increase 10/300 GL column (*GE*
375 *Healthcare Life Sciences*) in a buffer containing 20 mM HEPES, pH 7.4, 50 mM KCl, and
376 1 mM DDM. NaCl (100 mM) was added to the protein fractions immediately. The protein
377 was concentrated and supplemented with additional NaCl and ligands as needed. The
378 labeling efficiency was quantified using 1D NMR and found to be quantitative (**Fig. S1a**)

379

380

381 **Transport activity assay**

382 Unlabeled and mFE-labeled WT Glt_{Ph} were concurrently reconstituted into liposomes, and
383 initial rates of ^{3}H Asp uptake were measured as previously described [42]. Briefly, liposomes
384 were prepared from a 3:1 (w/w) mixture of *E. coli* polar lipids and egg yolk
385 phosphatidylcholine (*Avanti Polar Lipids*) in 20 mM HEPES/Tris, pH 7.4, containing 200
386 mM KCl and 100 mM choline chloride. Liposomes were destabilized by the addition of
387 Triton X-100 at detergent to lipid ratio of 0.5:1 (w/w). Glt_{Ph} proteins were added at a final
388 protein-to-lipid ratio of 1:2,000 (w/w) and incubated for 30 min at room temperature.
389 Detergents were removed with Bio-Beads™ SM-2 resin (*Bio-Rad*) via two incubations at
390 room temperature, one overnight incubation at 4 °C, and two more incubations at room
391 temperature. The proteoliposomes were concentrated to 50 mg/mL and flash-frozen in
392 liquid N_2. On the day of the experiment, liposomes were thawed and extruded through
393 400 nm filters. The uptake reaction was started by diluting the proteoliposomes 100-fold
394 into reaction buffer containing 20 mM HEPES/Tris pH 7.4, 200 mM KCl, 100 mM NaCl, 1
395 μM ^{3}H-L-Asp (*PerkinElmer*), and 0.5 μM valinomycin. Uptake was measured at 2 minutes
396 at 35 °C. Reactions were quenched by adding 10 volumes of cold buffer containing 20
397 mM HEPES/Tris pH 7.4, 200 mM KCl, and 100 mM LiCl. Uptakes of the mutants were
398 normalized to the WT protein in each experiment. Each data point is an average of at
399 least two technical replicates, and the data are composed of the results from three
400 independent liposome reconstitutions.

401 **^{19}F NMR spectroscopy**

402 ^{19}F NMR spectra were collected on Bruker Advance III HD 500 MHz spectrometer
403 equipped with a TCI ^{1}H-^{19}F/^{13}C/^{15}N triple resonance cryogenic probe (*Bruker Instruments*)
404 tuned for ^{19}F. For mFE-labeled proteins, 50 μM 2-fluoroethanol and 10 % D_2O were added
405 to the sample and used as a chemical shift reference (-224.22 ppm) and a lock signal,
406 respectively. Typically, 160 μl of the transporter solution at a final concentration of 100 -
407 250 μM (protomer) was loaded into a 4 mm Shigemi tube (Shigemi Co., Ltd). 1D ^{19}F NMR
408 spectra were recorded using the standard ZG pulse in the Bruker pulse library, with 2,096
409 points recorded and a spectral width (SW) of 40 ppm. The carrier frequency was set at -
410 220 ppm. The recycle delay was set to 1.5 and 0.9 s for deuterated and protonated mFE,

411 respectively, except when otherwise indicated. The scan numbers were set according to
412 protein and salt concentrations and temperatures between 2 and 30 K to achieve a
413 satisfactory signal-to-noise ratio. For tFE-labeled proteins, 50 μM trifluoroacetic acid was
414 added to the samples and used as a chemical shift reference (-76.55 ppm), the carrier
415 frequency was set at -70 ppm, and the recycle delay was set to 0.6 s. All the spectra were
416 recorded without decoupling.

417 All 1D ^{19}F NMR spectra were processed using MestReNova 12.0.0 software (*Mestrelab*
418 *Research*). The free induction decay signals were zero-filled to 8,192 points and Fourier-
419 transformed after applying a 20 Hz exponential window function. The spectra were
420 baseline-corrected, and the peaks were manually picked. The initial values of peak
421 heights and linewidths were manually set such that their sum approximated the original
422 spectrum. Simulated annealing was used for iterative fitting. During fitting, linewidths were
423 constrained between 20 and 800 Hz, peak positions were constrained within 5% variation,
424 and the peak shapes were set to Lorentzian. The reported linewidth values were obtained
425 by subtracting the line-broadening value of 20 Hz from the fitted linewidth. To test the
426 reliability of the fitting procedure and the reproducibility of the resulting parameters, we
427 recorded spectra of three independently prepared RSMR-M385C-mFE samples in 300
428 mM NaCl and 2 mM Asp. The obtained fitted values of chemical shifts, linewidths, and
429 state populations showed small standard deviations (**Fig. S3a-c, e**). Additionally, we
430 exported MestReNova-processed spectra and fitted them using the Multiple Peak Fit tool
431 in OriginPro 2019 software (*OriginLab*), which also reported small fitting errors (**Fig. S3d**).

432 ^{19}F longitudinal relaxation times (T_1) were measured by the inversion recovery method.
433 The recycle delays were set to 5 and 2.5 s for deuterated and protonated mFE probes,
434 respectively. The spectra were processed in MestReNova, imported into OriginPro
435 (*OriginLab*), and globally fitted using the Global Fit Tool patch. The peaks were picked,
436 and initial estimates of their chemical shifts, linewidths, and heights were set manually.
437 The chemical shift and linewidth values for each peak were held fixed between all spectra
438 in the relaxation series but varied relative to other peaks during fitting. The peak intensities
439 and areas were normalized using values obtained after the longest delay. T_1 relaxation

440 times were estimated by fitting the relaxation plots to single exponential functions $I =$
441 $I_0\left(1 - 2exp(-t/T_1)\right)$, where *I* is the normalized peak intensity, and *t* is the relaxation time.

442 To explore whether probe deuteration sharpens the resonance peaks as expected, we
443 compared the spectra of deuterated and protonated mFE attached to WT-M385C in the
444 presence of saturating Na^+ ions, where we observed well-resolved S3 and S4 peaks (**Fig.**
445 **S9**). Consistent with deuterium reducing the ^{19}F-^{1}H dipole relaxation and peak splitting
446 due to ^{19}F-^{1}H spin-spin coupling, deuterated mFE produced sharper peaks than
447 protonated mFE with a more pronounced effect on the intrinsically sharper S4 peak (**Fig.**
448 **S9**). However, the longer T_1 relaxation times (**Fig. S9**), increasing the recycle delay and
449 reducing sensitivity, offset the benefits of deuteration. If hardware enabling ^{1}H decoupling
450 during ^{19}F detection is available the protonated mFE probe might be preferable.

451 **Cryo-EM data collection**

452 To prepare cryo-grids, 3.5 µL of labeled Glt_{Ph} protein (4.5 mg/mL) was applied to a glow-
453 discharged QuantiFoil R1.2/1.3 300-mesh gold grid (*Quantifoil Micro Tools GmbH*) and
454 incubated for 2 min under 100 % humidity at the desired temperatures. Following
455 incubation, grids were blotted for 3 s at 0 blot force and plunge-frozen in liquid ethane
456 using a Vitrobot Mark IV (*Thermo Fisher Scientific*). Cryo-EM imaging data were acquired
457 on a Titan Krios microscope (*Thermo Fisher Scientific*) operated at 300 kV with a K3
458 Summit direct electron detector (*Gatan, Inc.*). Automated data collection was carried out
459 in superresolution mode with a magnification of 105,000 x, which corresponds to a
460 calibrated pixel size of 0.852 Å on the specimen and 0.426 Å for superresolution images.
461 An energy slit width of 20 eV was used throughout the collection. For the TBOA-bound
462 RSMR sample, movies were collected using Leginon [43] at a total dose of 52.88 $e^-/Å^2$
463 distributed over 48 frames (1.102 $e^-/Å^2$/frame) with an exposure time of 2.40 s (50
464 ms/frame) and a defocus range of 1.3 − 2.0 µm. A total of 8,100 movies were collected.
465 For the Asp-bound RSMR grids made at 4 °C, movies had a total dose of 50.94 $e^-/Å^2$
466 distributed over 48 frames (1.061 $e^-/Å^2$/frame) with an exposure time of 2.40 s (50
467 ms/frame) and a defocus range of 1.3 – 1.5 µm. A total of 5267 movies were collected.
468 For the Asp-bound RSMR grids prepared at 15 °C, movies had a total dose of 58.57 e^-
469 $/Å^2$ distributed over 50 frames (1.171 $e^-/Å^2$/frame) with an exposure time of 2 s (40

470 ms/frame) and a defocus range of 0.9 – 1.9 µm. A total of 14132 movies were collected.
471 For the Asp-bound RSMR grids prepared at 30 °C, movies had a total dose of 56.04 e^-
472 /$Å^2$ distributed over 40 frames (1.401 e^-/ $Å^2$/frame) with an exposure time of 1.6 s (40
473 ms/frame) and a defocus range of 1.3 – 1.6 µm. A total of 5823 movies were collected.

474 **Image processing**

475 The frame stacks were motion corrected using MotionCorr2 [44] with 2x binning, and
476 contrast transfer function (CTF) estimation was performed using CTFFIND4.1 [45]. Further
477 processing steps were carried out using RELION 3.0.8 or 3.1.0 and cryoSPARC 3.0 or
478 3.2 [46-47]. Particles were picked from micrographs using the Laplacian-of-Gaussian (LoG)
479 picker, aiming for ~2000 picks per micrograph. These particles were extracted using a
480 box size of 300 pixels with 4x binning and imported into cryoSPARC. Following one round
481 of 2D classification to remove artifacts, the particles underwent 3 rounds of
482 heterogeneous refinement in C1 using eight classes. Seven classes were noise volumes
483 created by one iteration of *ab initio*, and one was an unmasked 3D volume obtained from
484 a complete *ab initio* run. The particles were converted to Relion format using PyEM [48] and
485 re-extracted at full box size. These particles were reimported into cryoSPARC and
486 underwent one round of nonuniform (NU) refinement using C3 symmetry [49]. These
487 particles were converted back to Relion format for Bayesian polishing with parameters
488 obtained using 5,000 random particles [50]. The polished particles were reimported into
489 cryoSPARC and subjected to one round of NU refinement in C3 with both local and global
490 CTF refinement options turned on. The particles were again polished in Relion using an
491 expanded box size of 384 pixels, reimported into cryoSPARC, and subjected to one round
492 of NU refinement with C3 symmetry and local and global CTF refinement options turned
493 on. The particles were then C3 symmetry-expanded and subjected to a focused 3D
494 classification in Relion. The local mask was generated by UCSF Chimera[51] using a
495 combination of OFS (chain A of PDB model 2NWX) and IFS (chain A of PDB model
496 3KBC). The T value was set between 10 and 40 depending on the job. The 3D class
497 populations were calculated by dividing the particle number in the individual class or a
498 group of similar classes by the total number of C3 symmetry-expanded particles. The
499 particles from the individual classes or combined similar classes were imported

separately into cryoSPARC and subjected to local refinement using the mask and map obtained from the most recent NU refinement.

Model building and refinement

Crystal or cryo-EM structures were used as initial models and docked into the density maps using UCSF Chimera. The models were first real-space refined in PHENIX[52]. Misaligned regions were manually rebuilt, and missing side chains and residues were added in COOT[53]. Models were iteratively refined with applied secondary structure restraints and validated using MolProbity[54]. To cross-validate models, all atoms in the refined models were randomly displaced by an average of 0.3 Å, and each resulting model was refined against the first half-map obtained from processing. The FSC between the refined models and the first half-maps was calculated and compared to the FSC of the other half-maps. The resulting FSC curves were similar, showing no evidence of overfitting (**Fig. S10**). The structural figures were prepared in UCSF Chimera and PyMOL (DeLano Scientific).

Acknowledgments

The authors thank Dr. M. Goger and Dr. S. Bhattacharya for their help with setting up NMR. We thank Dr. B. Wang, Dr. A. Paquette, and Dr. W. Rice at the NYU cryo-EM facility for help with electron microscopy data collection. We also thank W. Eng and E. Wu for assistance with protein expression, and Dr. Z. Shen for assistance with chemical synthesis. This work was supported by NIH grants R37NS085318 and R01NS064357 (O.B.), R37AG019391 and R35 GM136686 (D.E.), and S10OD016320 (C.B.). O.B., D.E., and C.B. are members of the New York Structural Biology Center (NYSBC), which is supported in part by NIH Grant P41 GM118302 (CoMD/NMR: Center on Macromolecular Dynamics by NMR Spectroscopy), ORIP/NIH facility improvement grant CO6RR015495 and NIH grant S10OD018509.

Author contributions

Y.H., D.E., and O.B. designed the experiments; Y.H. performed the NMR experiments; Y.H. and O.B analyzed the data; C.B. assisted with NMR experimental data collection and analysis; Y. H and W. Z conducted the chemical synthesis; Y. H., K. R. and B. Q.

529 performed cryo-EM imaging, analyzed data, and refined molecular models; K. R.
530 performed transport activity assays; Y.H., K. R., O.B. and D.E. wrote the manuscript.

531 **Competing interests**

532 The authors declare no competing interests.

533 **References**

534 1. Lee, Y.; Lazim, R.; Macalino, S. J. Y.; Choi, S., Importance of protein dynamics in
535 the structure-based drug discovery of class A G protein-coupled receptors (GPCRs). *Curr.*
536 *Opin. Struct. Biol.* **2019,** *55*, 147-153.
537 2. Peng, J. W., Communication Breakdown: Protein Dynamics and Drug Design.
538 *Structure* **2009,** *17*, 319-320.
539 3. Sekhar, A.; Kay, L. E., An NMR View of Protein Dynamics in Health and Disease.
540 *Annu. Rev. Biophys.* **2019,** *48*, 297-319.
541 4. Palmer, A. G., NMR Characterization of the Dynamics of Biomacromolecules.
542 *Chem. Rev.* **2004,** *104*, 3623-3640.
543 5. Lerner, E.; Cordes, T.; Ingargiola, A.; Alhadid, Y.; Chung, S.; Michalet, X.; Weiss,
544 S., Toward dynamic structural biology: Two decades of single-molecule Förster
545 resonance energy transfer. *Science* **2018,** *359,* 288.
546 6. Lewis, J. H.; Lu, Z., Resolution of ångström-scale protein conformational changes
547 by analyzing fluorescence anisotropy. *Nat. Struct. Mol. Biol.* **2019,** *26*, 802-807.
548 7. Heath, G. R.; Scheuring, S., Advances in high-speed atomic force microscopy (HS-
549 AFM) reveal dynamics of transmembrane channels and transporters. *Curr. Opin. Struct.*
550 *Biol.* **2019,** *57*, 93-102.
551 8. Danielson, M. A.; Falke, J. J., Use of ^{19}F NMR to probe protein structure and
552 conformational changes. *Annu. Rev. Biophys. Biomol. Struct.* **1996,** *25*, 163-95.
553 9. Didenko, T.; Liu, J. J.; Horst, R.; Stevens, R. C.; Wuthrich, K., Fluorine-19 NMR of
554 integral membrane proteins illustrated with studies of GPCRs. *Curr. Opin. Struct. Biol.*
555 **2013,** *23*, 740-747.
556 10. Di Pietrantonio, C.; Pandey, A.; Gould, J.; Hasabnis, A.; Prosser, R. S.,
557 Understanding Protein Function Through an Ensemble Description: Characterization of
558 Functional States by ^{19}F NMR. In *Methods Enzymol.* **2019**, 615, 103-130.
559 11. Picard, L. P.; Prosser, R. S., Advances in the study of GPCRs by ^{19}F NMR. *Curr.*
560 *Opin. Struct. Biol.* **2021,** *69*, 169-176.
561 12. Suzuki, Y.; Brender, J. R.; Soper, M. T.; Krishnamoorthy, J.; Zhou, Y.; Ruotolo, B.
562 T.; Kotov, N. A.; Ramamoorthy, A.; Marsh, E. N. G., Resolution of Oligomeric Species
563 during the Aggregation of Aβ1–40 Using ^{19}F NMR. *Biochemistry* **2013,** *52*, 1903-1912.
564 13. Zhu, W.; Guseman, A. J.; Bhinderwala, F.; Lu, M.; Su, X. C.; Gronenborn, A. M.,
565 Visualizing Proteins in Mammalian Cells by ^{19}F NMR Spectroscopy. *Angew. Chem. Int.*
566 *Ed. Engl.* **2022,** *61*, e202201097.
567 14. Buchholz, C. R.; Pomerantz, W. C. K., ^{19}F NMR viewed through two different
568 lenses: ligand-observed and protein-observed ^{19}F NMR applications for fragment-based
569 drug discovery. *RSC Chem. Biol.* **2021,** *2* (5), 1312-1330.

15. Rashid, S.; Lee, B. L.; Wajda, B.; Spyracopoulos, L., Side-Chain Dynamics of the Trifluoroacetone Cysteine Derivative Characterized by ^{19}F NMR Relaxation and Molecular Dynamics Simulations. *J. Phys. Chem. B* **2019,** *123*, 3665-3671.
16. Manglik, A.; Kim, T. H.; Masureel, M.; Altenbach, C.; Yang, Z.; Hilger, D.; Lerch, M. T.; Kobilka, T. S.; Thian, F. S.; Hubbell, W. L.; Prosser, R. S.; Kobilka, B. K., Structural Insights into the Dynamic Process of β_2-Adrenergic Receptor Signaling. *Cell* **2015,** *161*, 1101-1111.
17. Ye, L.; Larda, S. T.; Frank Li, Y. F.; Manglik, A.; Prosser, R. S., A comparison of chemical shift sensitivity of trifluoromethyl tags: optimizing resolution in ^{19}F NMR studies of proteins. *J. Biomol. NMR* **2015,** *62*, 97-103.
18. Liu, J. J.; Horst, R.; Katritch, V.; Stevens, R. C.; Wuthrich, K., Biased signaling pathways in β_2-adrenergic receptor characterized by ^{19}F-NMR. *Science* **2012,** *335*, 1106-10.
19. Frei, J. N.; Broadhurst, R. W.; Bostock, M. J.; Solt, A.; Jones, A. J. Y.; Gabriel, F.; Tandale, A.; Shrestha, B.; Nietlispach, D., Conformational plasticity of ligand-bound and ternary GPCR complexes studied by ^{19}F NMR of the beta1-adrenergic receptor. *Nat. Commun.* **2020,** *11*, 669.
20. Huang, Y.; Wang, X.; Lv, G.; Razavi, A. M.; Huysmans, G. H. M.; Weinstein, H.; Bracken, C.; Eliezer, D.; Boudker, O., Use of paramagnetic ^{19}F NMR to monitor domain movement in a glutamate transporter homolog. *Nat. Chem. Biol.* **2020,** *16*, 1006-1012.
21. Boeszoermenyi, A.; Chhabra, S.; Dubey, A.; Radeva, D. L.; Burdzhiev, N. T.; Chanev, C. D.; Petrov, O. I.; Gelev, V. M.; Zhang, M.; Anklin, C.; Kovacs, H.; Wagner, G.; Kuprov, I.; Takeuchi, K.; Arthanari, H., Aromatic ^{19}F-^{13}C TROSY: a background-free approach to probe biomolecular structure, function, and dynamics. *Nat. Methods* **2019,** *16*, 333-340.
22. Ycas, P. D.; Wagner, N.; Olsen, N. M.; Fu, R.; Pomerantz, W. C. K., 2-Fluorotyrosine is a valuable but understudied amino acid for protein-observed ^{19}F NMR. *J. Biomol. NMR* **2020,** *74*, 61-69.
23. Wang, X.; Zhao, W.; Al-Abdul-Wahid, S.; Lu, Y.; Cheng, T.; Madsen, J. J.; Ye, L., Trifluorinated Keto-Enol Tautomeric Switch in Probing Domain Rotation of a G Protein-Coupled Receptor. *Bioconjug. Chem.* **2021,** *32*, 99-105.
24. de Dios, A. C.; Oldfield, E., Evaluating ^{19}F Chemical Shielding in Fluorobenzenes: Implications for Chemical Shifts in Proteins. *J. Am. Chem. Soc.* **1994,** *116*, 7453-7454.
25. Feeney, J.; McCormick, J. E.; Bauer, C. J.; Birdsall, B.; Moody, C. M.; Starkmann, B. A.; Young, D. W.; Francis, P.; Havlin, R. H.; Arnold, W. D.; Oldfield, E., ^{19}F Nuclear Magnetic Resonance Chemical Shifts of Fluorine Containing Aliphatic Amino Acids in Proteins: Studies on Lactobacillus casei Dihydrofolate Reductase Containing (2S,4S)-5-Fluoroleucine. *J. Am. Chem. Soc.* **1996,** *118*, 8700-8706.
26. Beguin, C. G.; Dupeyre, R., Nuclear spin relaxation in benzyl fluoride. I. 2H relaxation for internal rotational barrier determination and ^{1}H and ^{19}F intra- and intermolecular relaxation in pure benzyl fluoride. *J. Magn. Reson.* **1981,** *44*, 294-313.
27. Grage, S. L.; Durr, U. H.; Afonin, S.; Mikhailiuk, P. K.; Komarov, I. V.; Ulrich, A. S., Solid state ^{19}F NMR parameters of fluorine-labeled amino acids. Part II: aliphatic substituents. *J. Magn. Reson.* **2008,** *191*, 16-23.
28. Drew, D.; Boudker, O., Shared Molecular Mechanisms of Membrane Transporters. *Ann. Rev. Biochem.* **2016**, 85, 543-572.

616 29. Yernool, D.; Boudker, O.; Folta-Stogniew, E.; Gouaux, E., Trimeric Subunit
617 Stoichiometry of the Glutamate Transporters from *Bacillus caldotenax* and *Bacillus*
618 *stearothermophilus*. *Biochemistry* **2003,** *42*, 12981-12988.
619 30. Ruan, Y.; Miyagi, A.; Wang, X.; Chami, M.; Boudker, O.; Scheuring, S., Direct
620 visualization of glutamate transporter elevator mechanism by high-speed AFM. *Proc. Natl.*
621 *Acad. Sci. U.S.A*. **2017,** *114*, 1584-1588.
622 31. Akyuz, N.; Georgieva, E. R.; Zhou, Z.; Stolzenberg, S.; Cuendet, M. A.; Khelashvili,
623 G.; Altman, R. B.; Terry, D. S.; Freed, J. H.; Weinstein, H.; Boudker, O.; Blanchard, S. C.,
624 Transport domain unlocking sets the uptake rate of an aspartate transporter. *Nature* **2015,**
625 *518*, 68-73.
626 32. Huysmans, G. H. M.; Ciftci, D.; Wang, X.; Blanchard, S. C.; Boudker, O., The high-
627 energy transition state of the glutamate transporter homologue GltPh. *EMBO J.* **2021,** *40*,
628 e105415.
629 33. Kenyon, G. L.; Bruice, T. W., Novel sulfhydryl reagents. *Methods Enzymol.* **1977**,
630 47, 407-430.
631 34. Wang, X.; Boudker, O., Large domain movements through the lipid bilayer mediate
632 substrate release and inhibition of glutamate transporters. *eLife* **2020,** *9*, e58417.
633 35. Erkens, G. B.; Hänelt, I.; Goudsmits, J. M. H.; Slotboom, D. J.; van Oijen, A. M.,
634 Unsynchronised subunit motion in single trimeric sodium-coupled aspartate transporters.
635 *Nature* **2013,** *502*, 119.
636 36. Yernool, D.; Boudker, O.; Jin, Y.; Gouaux, E., Structure of a glutamate transporter
637 homologue from Pyrococcus horikoshii. *Nature* **2004,** *431*, 811-818.
638 37. Reddy, K. D.; Ciftci, D.; Scopelliti, A.; Boudker, O., Heterogeneous substrate
639 binding in a glutamate transporter homologue. *J. Gen. Physiol.* **2021**, 154, e202213131.
640 38. Geraets, J. A.; Pothula, K. R.; Schröder, G. F., Integrating cryo-EM and NMR data.
641 *Curr. Opin. Struct. Biol.* **2020,** *61*, 173-181.
642 39. Kwon, D. H.; Zhang, F.; Suo, Y.; Bouvette, J.; Borgnia, M. J.; Lee, S.-Y., Heat-
643 dependent opening of TRPV1 in the presence of capsaicin. *Nat. Struct. Mol. Biol.* **2021,**
644 *28*, 554-563.
645 40. Gao, J.; Liang, E.; Ma, R.; Li, F.; Liu, Y.; Liu, J.; Jiang, L.; Li, C.; Dai, H.; Wu, J.;
646 Su, X.; He, W.; Ruan, K., Fluorine Pseudocontact Shifts Used for Characterizing the
647 Protein-Ligand Interaction Mode in the Limit of NMR Intermediate Exchange. *Angew.*
648 *Chem. Int. Ed. Engl.* **2017,** *56*, 12982-12986.
649 41. Huang, S. K.; Pandey, A.; Tran, D. P.; Villanueva, N. L.; Kitao, A.; Sunahara, R.
650 K.; Sljoka, A.; Prosser, R. S., Delineating the conformational landscape of the adenosine
651 A_{2A} receptor during G protein coupling. *Cell* **2021,** *184*, 1884-1894.
652 42. Boudker, O.; Ryan, R. M.; Yernool, D.; Shimamoto, K.; Gouaux, E., Coupling
653 substrate and ion binding to extracellular gate of a sodium-dependent aspartate
654 transporter. *Nature* **2007,** *445*, 387-93.
655 43. Suloway, C.; Pulokas, J.; Fellmann, D.; Cheng, A.; Guerra, F.; Quispe, J.; Stagg,
656 S.; Potter, C. S.; Carragher, B., Automated molecular microscopy: the new Leginon
657 system. *J. Struct. Biol.* **2005,** *151*, 41-60.
658 44. Zheng, S. Q.; Palovcak, E.; Armache, J. P.; Verba, K. A.; Cheng, Y.; Agard, D. A.,
659 MotionCor2: anisotropic correction of beam-induced motion for improved cryo-electron
660 microscopy. *Nat. Methods* **2017,** *14*, 331-332.

661 45. Rohou, A.; Grigorieff, N., CTFFIND4: Fast and accurate defocus estimation from
662 electron micrographs. *J. Struct. Biol.* **2015,** *192*, 216-21.
663 46. Zivanov, J.; Nakane, T.; Forsberg, B. O.; Kimanius, D.; Hagen, W. J.; Lindahl, E.;
664 Scheres, S. H., New tools for automated high-resolution cryo-EM structure determination
665 in RELION-3. *Elife* **2018,** *7*, e42166
666 47. Punjani, A.; Rubinstein, J. L.; Fleet, D. J.; Brubaker, M. A., cryoSPARC: algorithms
667 for rapid unsupervised cryo-EM structure determination. *Nat. Methods* **2017,** *14*, 290-296.
668 48. Asarnow, D., Palovcak, E., Cheng, Y. UCSF pyem Zenodo
669 https://doi.org/10.5281/zenodo.3576630 (2019).
670 49. Punjani, A.; Zhang, H.; Fleet, D. J., Non-uniform refinement: adaptive
671 regularization improves single-particle cryo-EM reconstruction. *Nat. Methods* **2020,** *17*
672 1214-1221.
673 50. Zivanov, J.; Nakane, T.; Scheres, S. H. W., A Bayesian approach to beam-induced
674 motion correction in cryo-EM single-particle analysis. *IUCrJ* **2019,** *6*, 5-17.
675 51. Pettersen, E. F.; Goddard, T. D.; Huang, C. C.; Couch, G. S.; Greenblatt, D. M.;
676 Meng, E. C.; Ferrin, T. E., UCSF Chimera-A visualization system for exploratory research
677 and analysis. *J. Comput. Chem.* **2004,** *25*, 1605-1612.
678 52. Afonine, P. V.; Grosse-Kunstleve, R. W.; Chen, V. B.; Headd, J. J.; Moriarty, N.
679 W.; Richardson, J. S.; Richardson, D. C.; Urzhumtsev, A.; Zwart, P. H.; Adams, P. D.,
680 Phenix.model_vs_data: a high-level tool for the calculation of crystallographic model and
681 data statistics. *J. Appl. Crystallogr.* **2010,** *43*, 669-676.
682 53. Emsley, P.; Lohkamp, B.; Scott, W. G.; Cowtan, K., Features and development of
683 Coot. *Acta Crystallogr. D Biol. Crystallogr.* **2010,** *66*, 486-501.
684 54. Chen, V. B.; Arendall, W. B., 3rd; Headd, J. J.; Keedy, D. A.; Immormino, R. M.;
685 Kapral, G. J.; Murray, L. W.; Richardson, J. S.; Richardson, D. C., MolProbity: all-atom
686 structure validation for macromolecular crystallography. *Acta Crystallogr. D Biol.*
687 *Crystallogr.* **2010,** *66*, 12-21.

688

689 **Table of Contents (TOC)**

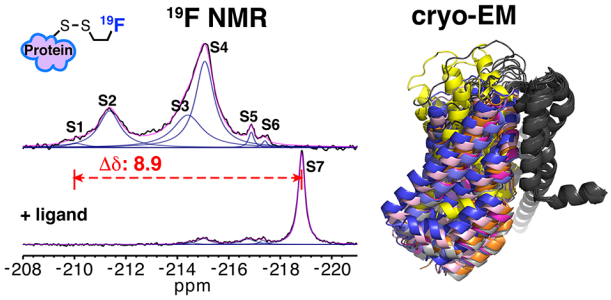

690

691